Impact of composition and crystallization behavior of atomic layer deposited strontium titanate films on the resistive switching of Pt/STO/TiN devices

N. Aslam, V. Longo, C. Rodenbücher, F. Roozeboom, W. M. M. Kessels, K. Szot, R. Waser, and S. Hoffmann-Eifert

Citation: Journal of Applied Physics **116**, 064503 (2014); doi: 10.1063/1.4891831
View online: http://dx.doi.org/10.1063/1.4891831
View Table of Contents: http://scitation.aip.org/content/aip/journal/jap/116/6?ver=pdfcov
Published by the AIP Publishing

Impact of composition and crystallization behavior of atomic layer deposited strontium titanate films on the resistive switching of Pt/STO/TiN devices

N. Aslam,[1,a)] V. Longo,[2,a)] C. Rodenbücher,[1,b)] F. Roozeboom,[2] W. M. M. Kessels,[2] K. Szot,[1] R. Waser,[1] and S. Hoffmann-Eifert[1,c)]
[1]*Peter-Grünberg Institute (PGI-7), Forschungszentrum Jülich and JARA-FIT, 52425 Jülich, Germany*
[2]*Department of Applied Physics, Eindhoven University of Technology, 5600 MB Eindhoven, The Netherlands*

(Received 8 April 2014; accepted 21 July 2014; published online 12 August 2014)

The resistive switching (RS) properties of strontium titanate ($Sr_{1+x}Ti_{1+y}O_{3+(x+2y)}$, STO) based metal-oxide-metal structures prepared from industrial compatible processes have been investigated focusing on the effects of composition, microstructure, and device size. Metastable perovskite STO films were prepared on Pt-coated Si substrates utilizing plasma-assisted atomic layer deposition (ALD) from cyclopentadienyl-based metal precursors and oxygen plasma at 350 °C, and a subsequent annealing at 600 °C in nitrogen. Films of 15 nm and 12 nm thickness with three different compositions [Sr]/([Sr] + [Ti]) of 0.57 (Sr-rich STO), 0.50 (stoichiometric STO), and 0.46 (Ti-rich STO) were integrated into Pt/STO/TiN crossbar structures with sizes ranging from 100 μm^2 to 0.01 μm^2. Nano-structural characterizations revealed a clear effect of the composition of the as-deposited STO films on their crystallization behavior and thus on the final microstructures. Local current maps obtained by local-conductivity atomic force microscopy were in good agreement with local changes of the films' microstructures. Correspondingly, also the initial leakage currents of the Pt/STO/TiN devices were affected by the STO compositions and by the films' microstructures. An electroforming process set the Pt/STO/TiN devices into the ON-state, while the forming voltage decreased with increasing initial leakage current. After a RESET process under opposite voltage has been performed, the Pt/STO/TiN devices showed a stable bipolar RS behavior with non-linear current-voltage characteristics for the high (HRS) and the low (LRS) resistance states. The obtained switching polarity and nearly area independent LRS values agree with a filamentary character of the RS behavior according to the valence change mechanism. The devices of 0.01 μm^2 size with a 12 nm polycrystalline stoichiometric STO film were switched at a current compliance of 50 μA with voltages of about ±1.0 V between resistance states of about 40 kΩ (LRS) and 1 MΩ (HRS). After identification of the influences of the films' microstructures, i.e., grain boundaries and small cracks, the remaining RS properties could be ascribed to the effect of the [Sr]/([Sr] + [Ti]) composition of the ALD STO thin films. © *2014 AIP Publishing LLC*.
[http://dx.doi.org/10.1063/1.4891831]

I. INTRODUCTION

The increasing importance of advanced information technology drives the searching for an energy-efficient, non-volatile memory device with high integration density, fast access time, high endurance, and sufficient data retention. Among alternative concepts which are discussed for future replacement of today's dynamic random access memory (DRAM) and flash memory, the redox-based memristive device (ReRAM) is one of the most promising concepts.[1] ReRAM basically consists of an insulator (e.g., a metal oxide) sandwiched between two metal electrodes (M, M′) (metal electrodes), and the information is stored in form of at least two or even multilevel resistance states.[2] The reversible switching between the different resistance states is induced by a certain voltage signal V_{SET} which sets the device to the low resistance state (LRS or ON-state) and V_{RESET} which resets the device to the high resistance state (HRS or OFF-state). For ReRAM applications, a resistance ratio $R_{OFF}/R_{ON} > 10$ is required, while absolute values in the MΩ range guarantee low power operation. Among the class of resistive switching (RS) materials, transition metal oxides are attracting increasing interest.[3,4]

For a wide range of metal oxides, the valence change memory effect (VCM) occurs, characterized by a migration of oxygen anions (or corresponding oxygen vacancies), typically over a length of a few nanometers. The local change of the metal to oxygen stoichiometry results in a nanoionic redox reaction and a valence change of the cation sublattice leading to a change in the electronic conductivity. The VCM effect is a bipolar-type RS, where the polarity of the applied voltage determines the direction of the redox reaction, i.e., reduction (SET) or oxidation (RESET).[5] Basically, VCM cells consist of an active electrode, at which the RS takes place, a mixed ionic-electronic conducting (MIEC) layer, and an ohmic reference electrode from a material of higher

[a)]N. Aslam and V. Longo contributed equally to this work.
[b)]C. Rodenbücher performed the AFM and LC-AFM analysis.
[c)]Electronic mail: su.hoffmann@fz-juelich.de

oxygen affinity as compared with the active electrode. The active (switching) interface will form between the MIEC layer and the active electrode with the low oxygen affinity and high work function. In most M/O/M′ stacks with a single oxide layer (O), an electroforming (EF) process at higher voltages V_{form} is required before stable bipolar RS can be obtained. In today's understanding of the VCM-type RS phenomena, the electroforming process locally removes oxygen ions from the insulating oxide lattice, providing semiconducting filamentary type paths which allow the high current flow.[5] High forming voltages are undesirable because they are not applicable to integrated devices[6] and because of the large material reconstruction which is induced by the high power applied to the device.[7] The RS behavior of a device under study depends strongly on the performed EF procedure which needs therefore to be discussed along with the RS characteristics themselves.

Towards the industrial application of ReRAM devices, vertical cross point architectures (VCPA) are intensively discussed for reaching the extreme high integration density required for future memory devices. Therefore, atomic layer deposition (ALD) will be the preferred deposition technique for the preparation of thin films on such three-dimensional structures. The utilization of ALD processes for ReRAM fabrication so far is basically limited to a few binary oxides, like HfO_2,[8,9] Al_2O_3,[10] and TiO_2[11,12] grown in amorphous or nano-crystalline form. While only a few studies deal with binary oxide single crystalline material, for example, in Refs. 13 and 14.

In this work, the use of ALD for ReRAM is extended to $Sr_{1+x}Ti_{1+y}O_{3+(x+2y)}$ (STO), a ternary oxide, where the composition of the films can be tuned by the ALD processing parameters. Main focus was on the effect of the cation ratio [Sr]/([Sr] + [Ti]) on the RS performance, because of two reasons. First, the STO composition has a significant effect on the leakage current properties of M/STO/M′ capacitors.[15] Second, stoichiometry effects in the RS phenomena of epitaxial STO structures grown by pulsed laser deposition (PLD) at temperatures of typically 700 °C to 800 °C have been intensively studied.[16] These might serve as a good comparison and therefore give insights on the RS of ALD STO films.[17]

The bipolar RS in epitaxial $SrTiO_3$ thin film devices is basically attributed to an electric field and temperature-enhanced drift of oxygen vacancies along filaments which induces a metal-to-insulator transition in the $SrTiO_3$ material.[5,18,19] The confined nature of the conductive filaments in single-crystalline $SrTiO_3$ has been shown by Szot *et al.*[20] using local-conductivity atomic force microscopy (LC-AFM) with nanometer resolution. In addition to the filamentary-type RS, an area-dependent type of RS has been reported for epitaxial $SrTiO_3$ films by Muenstermann *et al.*[21] The corresponding *I-V* switching curves reveal two main differences regarding the switching polarity and the electrode area scaling behavior. It should be noted that the RS polarity is defined for a "standard" M/O/M′ configuration, when the voltage of the active electrode is displayed in the *I-V* curve.[5] With this definition, the "filamentary" type of RS is characterized by a "counter-eightwise" *I-V* characteristic, and it shows no significant contact area dependence while the "homogeneous" RS effect exhibits an "eightwise" switching polarity and a clear pad size dependence of the conducting LRS state. According to Muenstermann *et al.*,[21] both types of RS, filamentary and area switching, can coexist in the same epitaxial $SrTiO_3$ thin film, depending on the local defect density in the active switching regime. For PLD STO films, effects on the RS behavior by growth induced structural defects[22] and by variations in the cation stoichiometry[23] were reported. The studies on epitaxial STO thin films already showed that the control of the density and the distribution of defects are of utmost importance for the fabrication of reproducible and scalable resistive switching devices. An obstacle for the use of epitaxial STO layers is that they are grown by high temperature PLD processes on single crystalline oxide substrates. Both requirements are not compatible with high-density large-scale integration of up-to-date memory technologies.

In contrast, industrially relevant RS devices need to be integrated onto complementary metal oxide semiconductor (CMOS) chips in analogy to today's production of high-*k* layers in DRAMs[24,25] and in analog circuit applications.[26–28] The microstructure of integrated STO thin films is therefore expected to be amorphous, nano-crystalline, or even a mixture of the two. For the conformal growth on three dimensional (3D) structured devices with high integration density, chemical vapor deposition techniques[29,30] and, in particular, ALD techniques,[15,31,32] were utilized. Although the requirements on the aspect ratio of 3D structures for ReRAM applications are still moderate, the future of high-density ReRAM will also be defined by more challenging 3D topologies.[33]

In this study, we attempt to link fundamental knowledge about resistive switching mechanisms in single crystalline material with the same material grown in high quality by means of the ALD technique in order to identify key factors in the transfer from the "ideal" system design to the design of "real" structures. According to the previous works, thin film STO is a predestined material for this study. Therefore, a comprehensive analysis of the RS performance of capacitors built from ALD STO thin films was performed with a focus on the effects of films cation composition, microstructure, and morphology. While the [Sr]/([Sr] + [Ti]) ratio in the as-deposited amorphous films could be well controlled by means of the ALD pulsing sequence, the microstructure and morphology of the polycrystalline STO thin films were found to depend in a complex manner on various external parameters, like the substrate material, the cation stoichiometry, the film thickness, and the annealing conditions.[15,34] We will show that, in addition, the RS behavior of the ALD STO based device is affected by the [Sr]/([Sr] + [Ti]) composition and by the thin film's microstructure and morphology.

II. EXPERIMENTAL SECTION

12 and 15 nm thick $Sr_{1+x}Ti_{1+y}O_{3+(x+2y)}$ films with various cation compositions [Sr]/([Sr] + [Ti]) of 0.57 (Sr-rich), 0.50 (stoichiometric), and 0.46 (Ti-rich) were deposited by means of plasma-assisted ALD at 350 °C in an Oxford Instruments FlexAL reactor. Platinum coated silicon wafers

with a layer stack of Si/SiO_2 (430 nm)/Ti (5 nm)/Pt (30 nm) were used as substrates with the Pt bottom electrode (BE) in planar or bar-structured configuration. Cyclopentadienyl-based precursors from AirLiquide, namely, Ti-Star, (pentamethylcyclopenta-dienyl) tri-methoxy-titanium, $CpMe_5Ti(OMe)_3$, and Hyper-Sr, bis(tri-isopropylcyclopentadienyl)-strontium with a 1,2-dimethoxy-ethane adduct, $Sr(^iPr_3Cp)_2DME$, were used in sequence with oxygen plasma as the co-reactant. The [Sr]/([Sr] + [Ti]) ratios of the films were adjusted by tuning the [SrO]/[TiO_2] ALD cycle ratio, while the film thicknesses were controlled by the numbers of executed ALD cycles. Details on the growth process can be found in a recent publication.[35] For the determination of the thickness and the optical properties of the films grown on planar Si/Pt substrates, *ex-situ* spectroscopic ellipsometry (SE) measurements were performed on a J.A. Woollam/M2000D system (1.25–6.5 eV). The [Sr]/([Sr] + [Ti]) content of the as-deposited STO films was estimated from the optical properties of the thin films determined by SE employing a library calibrated by Rutherford backscattering measurements.[35] Additionally, the composition was determined from X-ray photoelectron spectroscopy (XPS) data taken with a Thermo Scientific K-Alpha spectrometer using monochromatic Al K_α X-ray radiation ($h\nu = 1486.6$ eV). Charge correction was performed by setting the C1s signal at a binding energy of 284.8 eV.[36] A post-deposition rapid thermal annealing (RTA) of the films at 600 °C in nitrogen atmosphere was performed for crystallization of the layers into the perovskite structure. The chemical and structural properties of the annealed films grown on planar Pt substrates were analyzed by means of XPS and by grazing-incidence X-ray diffractometry (GI-XRD) using a Panalytical X'Pert PRO MRD with Cu K_α radiation. In addition, the morphology of the annealed films was studied by scanning electron microscopy (SEM) using a Hitachi SU 8000 system. LC-AFM analyses were done with a Pt/Ir coated tip on a JEOL JSPM-5200 scanning probe microscope to record topography and current maps under ultra-high vacuum (UHV) conditions at 200 °C. For the resistive switching characterization, similar STO thin films were integrated into Pt/STO/TiN crossbar devices on Si/SiO_2 substrates. Schematics of the stack sequence and of the lateral structure together with two representative electron micrographs are shown in Figures 1(a)–1(d). The fabrication of the BE on (25×25 mm^2) silicon substrates with about 430 nm thermal oxide started by sputtering of 5 nm Ti and 30 nm Pt. A conventional photolithography process using a Mask Aligner MA6, Karl Suess was combined with reactive ion beam etching (RIBE) with argon plasma in an Oxford Ionfab 300 Plus system to pattern the micro-sized BE. For the nano-sized Pt BE, a structuring process was performed by UV nanoimprint lithography (NIL) using a Nanonex NX 2000 nanoimprinter and RIBE. In analogy to the planar structures, the STO thin films were grown by plasma-assisted ALD and subsequently annealed at 600 °C in flowing nitrogen for 10 min (15 nm) and 5 min (12 nm). The top electrodes (TE) of the micro-crossbar cells were prepared in a "*bottom-up*" approach as follows. First, the electrode structures were defined by photolithography. Then, a 30 nm thick TiN film was deposited by sputtering, and the TE was structured by a lift-off process. Last, the platinum BE of each device was opened for making an external electrical contact, again by means of photolithography and RIBE. A top-view SEM micrograph of the micro-crossbar structure is shown in Fig. 1(c). The TEs of the nano-crossbar cells were prepared in a "*top-down*" approach. First, 30 nm thick TiN was deposited by sputtering, second, the TE structures were defined by means of e-beam lithography using a Vistec EBPG 5000 plus system. Next, the TiN layer and the STO films underneath were patterned by means of RIBE with CF_4 plasma. A schematic and a scanning electron micrograph are given in Figs. 1(b) and 1(d). For both types of cross bar structures, the final stack sequence in the cross junction area consisted of the BE (5 nm Ti/30 nm Pt), the functional STO film of (15 or 12 nm), and the TE (30 nm TiN) as depicted in Fig. 1(a). The lateral dimensions of the active device areas ranged from (10×10) μm^2 to (1×1) μm^2, and (100×100)

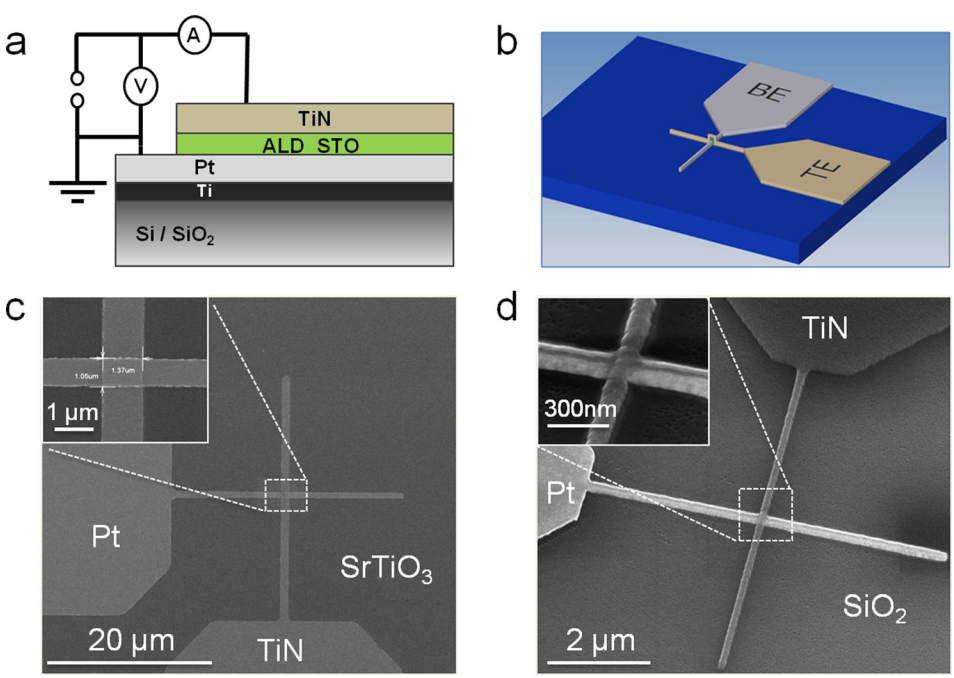

FIG. 1. (a) Stack sequence and electrical measurement setup of the Pt/STO/TiN devices. (b) Schematic picture of the nano-crossbar structures with the BE and the TE. In the "*top-down*" approach, the switching oxide layer only remained under the TE. (c) SEM micrographs of a micro-crossbar Pt/STO/TiN structure. In the "*bottom-up*" approach, the TiN TE is structured by a lift-off technique. (d) SEM micrographs of a nano-crossbar Pt/STO/TiN structure; the TiN and the STO underneath are structured by RIBE.

TABLE I. Cation stoichiometry of the STO films as-deposited on planar Si/Ti/Pt substrates given as a function of the ALD process parameters. The [Sr]/([Sr] + [Ti]) content ratios were determined by SE and cross-checked by XPS. The relative errors in the [Sr]/([Sr] + [Ti]) ratios from SE and XPS are ±0.03 and ±0.02, respectively.

STO composition	$(SrO)/(TiO_2)$ ALD cycle ratio	[Sr]/([Sr] + [Ti]) content ratio from SE	[Sr]/([Sr] + [Ti]) content ratio from XPS
Ti-rich	1: 4	0.46	0.46
stoichiometric	1: 3	0.50	0.50
Sr-rich	1: 2	0.57	0.58

nm^2, for the micro- and nano-crosspoint junctions, respectively. The current-voltage (*I-V*) characteristics were recorded in a quasi-static mode under ambient conditions using an Agilent B1500A semiconductor analyzer combined with a Suess Microtec PA-200 probe station. In the used configuration, the current-resolution of the setup was in the range of 1 pA. In the measurements of the Pt/STO/TiN crossbar devices, the voltage signal was always applied to the top electrode (TiN), while the bottom electrode (Pt) was grounded.

III. RESULTS AND DISCUSSION

A. Physical and chemical properties of STO films

The chemical composition and the thickness of as-deposited STO films on planar Si/Pt structures were characterized by means of SE and XPS. Further details on the characterization methods applied to comparable STO films grown on different substrates have been reported in Refs. 34, 35, and 37. Table I comprises the properties of the STO films which were used in this study. It should be mentioned that the planar Pt layers were deposited in exactly the same manner as the Pt bottom electrodes of the crossbar structures in order to assure identical ALD growth behavior of the STO films. Films of three different compositions were obtained, Ti-rich STO, stoichiometric STO, and Sr-rich STO with [Sr]/([Sr] + [Ti]) ratios of 0.46, 0.50, and 0.57, respectively.

The as-deposited amorphous films underwent a RTA step at 600 °C to achieve crystallization where the film thickness decreased to about 85–90% of the initial value. Although variations of the cation composition in the as-deposited amorphous films can be easily adjusted in ALD, induced effects on the film crystallization behavior might result in different microstructures for films of various compositions after crystallization. In addition, the incorporation of excess strontium or titanium oxide into the $SrTiO_3$ thin films is an issue.

High quality $SrTiO_3$ single crystals exhibit a rather low solubility limit for either excess SrO or excess TiO_2. Witek *et al.*[38] found for STO ceramics that a Ti excess of only 0.5 at% is sufficient to start the segregation of TiO_2. Depending on the oxygen content, not only TiO_2 but also various titanium suboxides might form.[39] In consequence, intergrowth of SrO layers or TiO_2 layers and the perovskite-type $SrTiO_3$ might occur. The intergrowth leads to the formation of either Ruddlesden-Popper (RP) phases for the Sr-rich STO material $(Sr_{n+1}Ti_nO_{3n+1})$[40,41] or Magnéli type-phases for the Ti-rich STO films $(Ti_nO_{2n-1})^*(SrTiO_3)$.[42,43]

Depending on the growth or annealing temperature, the mean free path of cations is limited, and therefore in the STO thin films, the ordered-fashion-type intergrowth might only happen on a local scale, leading to micro-regions of slightly different compositions.[41] The incorporation of cations in excess of the stoichiometric $SrTiO_3$ composition has been investigated for different ALD STO thin films used as high-*k* material.[15] Clima *et al.*[44] and Popovici *et al.*[32] studied the crystallization behavior of Sr-rich STO films grown by thermal ALD from $Sr(^tBu_3Cp)_2$ and $Ti(OMe)_4$. After RTA at 600 °C, the films showed perovskite-type reflections in XRD, while the peaks of the Sr-rich film are slightly shifted towards lower angle as compared with the stoichiometric film. This "low temperature metastable crystalline" state was transferred into a RP-type crystalline structure, $SrO(SrTiO_3)_n$, after annealing at about 1000 °C.[44] A similar result was reported by Shibuya *et al.*[45] showing that PLD grown Sr_2TiO_4 films exhibit a distribution of extended defects or a regular RP-phase structure depending on the growth temperature. In the resistive switching behavior of oxide devices, local imperfections and inhomogeneities in the thin film structure and morphology can play an important role. Therefore, the micro-structural properties of the 600 °C annealed ALD STO thin films were carefully analyzed.

Figure 2(a) shows the GI-XRD scans of 12 nm thick STO films of the three compositions annealed at 600 °C for 5 min. The spectra clearly reveal that despite the non-stoichiometry, all STO films appeared to crystallize into the metastable perovskite phase. The results are comparable with the previous reports on the micro-structural evolution of annealed ALD STO films.[15,27,32,35] For the metastable crystalline Sr-rich STO films, it is suggested that the excess SrO could be distributed randomly and in a disordered manner in the $SrTiO_3$ matrix. This picture might also apply to the

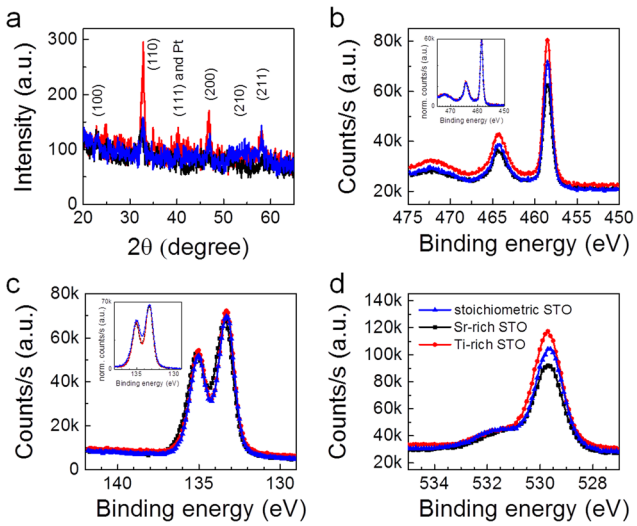

FIG. 2. Structural and chemical characterization of 12 nm thick STO films with different [Sr]/([Sr] + [Ti]) compositions according to Table I. The films were grown on planar Pt/Si substrates and annealed at 600 °C in nitrogen for 5 min, analog to the crossbar structures; (a) GI-XRD scans, (b)–(d) XPS spectra of the Ti 2p lines (b), the Sr 3d lines (c), and the O 1s lines (d).

metastable crystalline STO thin films of different stoichiometries investigated in this study.

Detailed photoelectron spectra of the Ti 2p, Sr 3d, and O 1s signals taken for the 12 nm thick STO films after annealing at 600 °C are shown in Figures 2(b)–2(d), respectively. The binding energies of Ti $2p_{3/2}$ of ~458.5 eV and of Sr $3d_{5/2}$ of ~133.3 eV found for all the three samples with different compositions are in good agreement to bulk reference data.[46] For a comparative analysis of the chemical states of the constitutive cations in the stoichiometric, Ti-rich and Sr-rich STO films, the photoelectron spectra for the Ti 2p and Sr 3d signals were normalized to the maximum intensity of the Ti $2p_{3/2}$ and Sr $3d_{5/2}$, respectively. The normalized patterns are given in the insets of the figures. The Ti 2p lines show the same valence states and FWHM values for all three STO compositions, while in general, the thin film signals reveal a broadening as compared with single crystal reference data indicating a higher degree of lattice disorder. The Sr 3d lines of the stoichiometric and the Ti-rich STO film are nearly identical, while for the Sr-rich STO, a broadening of the lines towards higher binding energies is observed, which indicates the formation of a Sr-carbonate compound in the near surface region. In addition, the O 1s signals show two features, a broad shoulder originating from carbonly-adsorbates on the surface and the O 1s peak at ~529.8 eV attributed to $SrTiO_3$. The intensity ratio of surface oxygen to bulk oxygen increases with increasing [Sr]/([Sr] + [Ti]) content. The formation of a strontium carbonate compound on the surface of the Sr-rich STO film agrees to a microscopic model of an intergrowth of SrO and $SrTiO_3$ layers in the Sr-rich STO films (0.57), where SrO in the near surface region will react to form $SrCO_3$ based compounds.

XRD and XPS analyses of the 600 °C annealed STO films revealed perovskite-type crystalline phases with contributions from intergrowth of excess-cation oxide. XPS data suggest the possibility of SrO intergrowth in the Sr-rich STO films. Although defined signals originating from TiO_{2-x} intergrowth in the Ti-rich STO films were not observed, the broadening of the Ti 2p lines might indicate additional Ti oxidation states.

B. Thin film microstructure and morphology

The microstructure and the morphology of the plasma-assisted ALD STO thin films after annealing at 600 °C were analyzed with respect to the different compositions and film thicknesses. The thin film crystallization is controlled by the kinetics of nucleation and grain growth. On similar thin films deposited on Si_3N_4 grids, Longo *et al.*[34] showed by means of transmission electron microscopy (TEM) that the crystallization of the films yielded transrotational perovskite-type crystals. In addition, the important effect of the STO composition and the annealing temperature on the final grain size, the crack, and the void formation has been demonstrated. In particular, the regular small-grain morphology of the crystalline Sr-rich STO films was imputed to a high nucleation probability at the onset of crystallization process.

The microstructural characterizations were performed on STO thin films of Sr-rich (0.57), stoichiometric (0.50) and Ti-rich (0.46) composition deposited on planar Si/Pt substrates after annealing at 600 °C in nitrogen for about 5 min (12 nm) and 10 min (15 nm). Figure 3 displays the plan-view high resolution SEM top view micrographs of the annealed STO thin films. The graphs of the 15 nm thick STO films are shown in Figs. 3(a)–3(c) and those of the 12 nm films are given in Figs. 3(d) and 3(e). The micrographs are arranged from left to right with respect to a decreasing Sr-content, in particular, Sr-rich STO (0.57), stoichiometric STO (0.50), and Ti-rich STO (0.46). The Sr-rich and the stoichiometric composition each show a comparable surface morphology for the films of different thicknesses, while grain boundaries appear more pronounced in the 15 nm thick STO films as compared with 12 nm thick films. The Sr-rich STO films (Figs. 3(a) and 3(d)) exhibit a finer grained structure with a

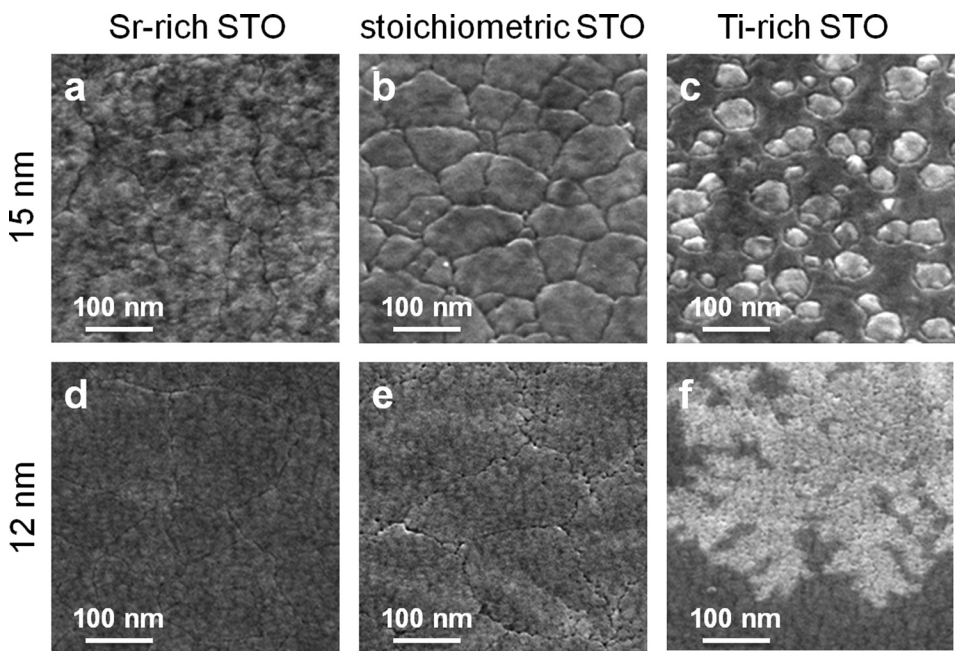

FIG. 3. SEM top view micrographs of STO thin films of different [Sr]/([Sr] + [Ti]) compositions grown on planar Si/Pt substrates after annealing at 600 °C in nitrogen; (a)–(c) 15 nm films annealed for 10 min, (d)–(f) 12 nm films annealed for 5 min; the STO compositions are arranged from the left to the right Sr-rich (a) and (d), stoichiometric (b) and (e), and Ti-rich (c) and (f).

more uniform morphology compared with the stoichiometric films (see Figs. 3(b) and 3(e)), where grid-patterns indicate small cracks formed at the grain boundaries upon crystallization and consequent densification (see also Ref. 34). The cracks seem less pronounced for the Sr-rich films. This is consistent with the previous TEM study[34] which revealed an increased nucleation density leading to a higher density of smaller grains for the Sr-rich films as compared with the stoichiometric STO films. The Ti-rich STO films showed altogether a different surface morphology. Regimes of different contrast with a lateral extension of about 100 nm–500 nm are revealed in the SEM micrographs (Figs. 3(c) and 3(f)). Referring to previous crystallization studies,[34] the morphological differences were explained by a locally incomplete crystallization process. In particular, additional AFM analyses (see Fig. 4(c)) revealed the brighter contrast regions being about 10% thinner compared with the surrounding darker regions. The reduced thickness is related to a densification process due to the crystallization. The different shapes of the crystallites between the films of 12 nm and 15 nm in thickness might relate to a thickness effect on the crystallization or to slight differences in composition. It has been shown that Ti-rich STO thin films require an increased thermal budget to achieve crystallization compared with stoichiometric and Sr-rich films.[34] Hence, slight differences in composition can lead to pronounced changes in the crystallization behavior of the Ti-rich films.

C. Local conductivity probed by LC-AFM

Morphological atomic force microscopy (AFM) and LC-AFM studies were performed in order to analyze local conducting paths along grains and grain boundaries. For this, the film's surface topography was recorded in parallel to a laterally resolved current mapping for the 12 nm thick STO films annealed for 5 min at 600 °C. The measurements were performed under UHV conditions at 200 °C while a constant voltage was applied to the sample via a conducting Pt/Ir-coated AFM tip. The AFM results shown in Figs. 4(a)–4(c) reveal distinct topographical differences between the three samples, with the surface of the Sr-rich (a) and the stoichiometric STO (b) film being rather flat and consisting of grains separated by grain boundaries. The corresponding current maps (Figs. 4(d)–4(f)) show an inhomogeneous distribution of differently conducting regimes. Although the averaged conductivity of the Sr-rich sample (Fig. 4(d)) was significantly lower than that of the stoichiometric STO (Fig. 4(e)), both films reveal conducting paths along grain boundaries. Small cracks in the stoichiometric STO film which appear in the topography map (Fig. 4(b)) as darker lines show up as slightly brighter lines in the LC-AFM map (Fig. 4(e)). The degree by which the nano- or microcracks contribute to the total leakage current of a device might depend on the dimensions of the cracks for each individual case. Comparable results on local leakage non-uniformity in ALD STO thin films have been reported by Menou *et al.*[15] who also attributed the higher leakage paths to micro-cracks in their films. The topography map of the partly crystallized Ti-rich STO film (([Sr]/([Sr] + [Ti]) = 0.46) in Fig. 4(c) looks completely different as for the other STO compositions. The corresponding current map in Fig. 4(f) shows that the thinner areas of the material exhibit increased conductivity indicating that semiconducting phases are formed locally in the Ti-rich STO films. One might notice the remarkable accordance between the AFM, LC-AFM, and SEM images with respect to the areas of reduced film thickness in Fig. 4(c) and these with enhanced conductivity in Fig. 4(f). Therefore, these regimes might be described by being large crystal plates of Ti-rich STO phase embedded in an insulating matrix of amorphous material. The assumption of partial crystallization is in

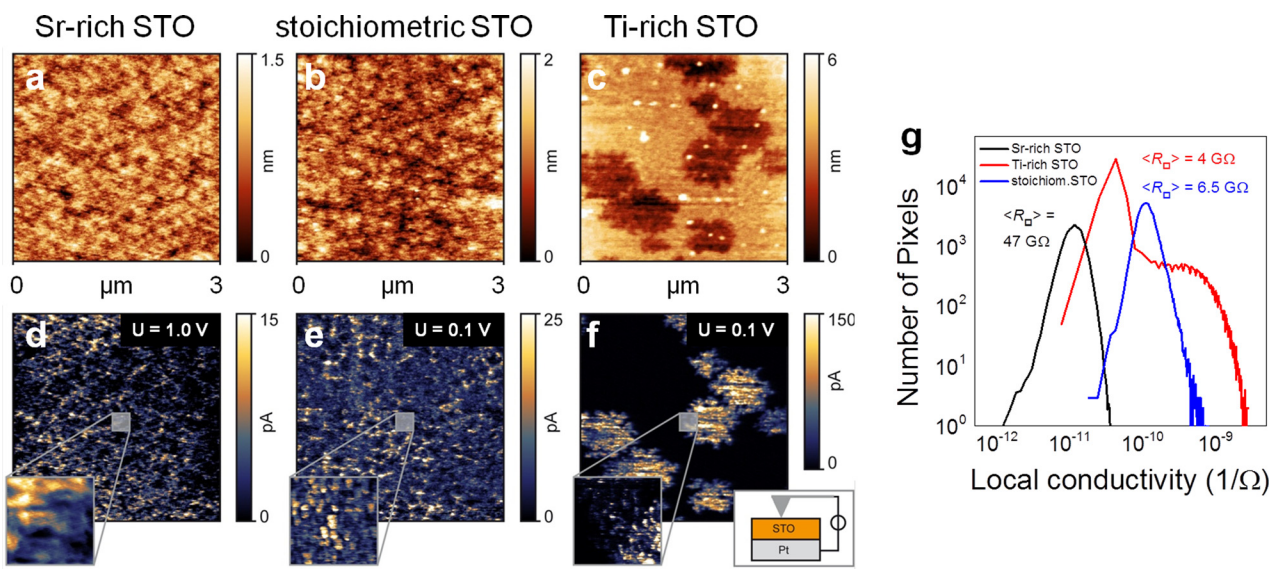

FIG. 4. (a)–(c) AFM and (d)–(f) LC-AFM pictures showing the topography and the corresponding current maps, respectively, of the 12 nm STO thin films grown on planar Si/Pt substrates and annealed for 5 min at 600 °C in nitrogen; the STO compositions are arranged from the left to the right Sr-rich (a) and (d), stoichiometric (b) and (e), and Ti-rich (c) and (f). The LC-AFM measurements were performed at 200 °C under UHV conditions with the voltage applied to the AFM tip. (g) Histogram of the local conductivity values shown in pictures (d)–(f). Average resistance values $<R_{\square}>$ refer to the measured areas of (3 × 3) μm^2.

qualitative agreement with the results of a recently performed TEM study,[34] while slight variations in the film growth might arise from the different substrates.

The LC-AFM results clearly reveal locally inhomogeneous current spots which relate to the thin film's microstructure being influenced by the film's composition as the result of a stoichiometry-affected nucleation and crystallization behavior. Thus, in order to interpret the electrical properties of the RS devices properly, both, the influence of the [Sr]/([Sr] + [Ti]) composition as well as the microstructure of the ALD STO thin films after annealing have to be considered. It should be mentioned that the above described microstructural phenomena particular appear on a length scale of a few hundred nanometers. Therefore, the electrical properties of the micro-crossbar structures present average thin film properties, whereas for the nano-crossbar devices with the pad size approaching the grain size, one would expect a slight statistical change in the electrical data. In the 100 nm regime, the pad might either cover a single grain or two grains with a grain boundary in between or, alternatively for the Ti-rich STO films, the pad could either sit on the amorphous, less conducting matrix, or on a semiconducting grain. In addition, the presence of a current inhomogeneity on the smaller scale could be observed by LC-AFM at higher resolution. The grains of the Sr-rich and stoichiometric STO (see Figs. 4(d) and 4(e)) revealed additional local conductivity spots with a diameter of 10 nm to 30 nm inside the grains. This observation agrees with the evidence of voids with diameter of a few nanometers within single STO grains found by TEM in our previous study.[34] Since the stoichiometry range of $SrTiO_3$ is very small, a phase separation in non-stoichiometric parts could also evolve. Hence, one possible explanation of the locally different conductivities observed by LC-AFM could be that in the investigated Ti-rich STO thin films, TiO_x-phases[47] were present influencing the local conductivity.

In the histogram in Fig. 4(g), the distribution of the local conductivity as measured by the LC-AFM scans in Figs. 4(d)–4(f) over an area of $3 \times 3\ \mu m^2$ is shown. The number of pixels is plotted logarithmically versus the local conductivity calculated from the measured current and the applied voltage, $\sigma_{loc} = I_{loc}/V_{tip}$. This allows a semi-quantitative discussion of the mean thin film resistance values $<R_{\square}>$. It can be seen that the average conductivity of the Sr-rich STO film was the lowest ($<R_{\square}> = 47\ G\Omega$) although a relatively high voltage of 1.0 V was applied to the sample, whereas for the stoichiometric STO film, a higher average conductivity was determined ($<R_{\square}> = 6.5\ G\Omega$) at a lower applied voltage of 0.1 V. The Sr-rich and the stoichiometric STO thin film both exhibit comparable unimodal conductivity distributions indicating that the distribution of conducting grains is similar in both cases despite the overall difference in conductivity. The histogram of the Ti-rich STO film instead shows a bimodal distribution relating to the two regions with different local conductivities. While a large part of the scanned area revealed a low local conductivity resulting in the appearance of the maximum peak in the histogram, the highly conducting areas in Fig. 4(f) are reflected by the tail of the distribution at higher conductivities. The width of the local conductivity distribution in the histogram is the highest for the Ti-rich sample due to the inhomogeneous distribution of conducting grains, while the mean value of the thin film resistance $<R_{\square}> = 4\ G\Omega$ is only slightly smaller than the value of the stoichiometric STO film.

D. Electrical properties of M/STO/M′ devices in the initial state

The effect of the [Sr]/([Sr] + [Ti]) composition on the dielectric properties of Pt/STO/Pt based devices obtained from 15 nm thick films annealed at 600 °C has been investigated in a previous study.[50] Mean values of the capacitance density were about 50 fF/μm^2, 25 fF/μm^2, and 10 fF/μm^2 for the stoichiometric, the Sr-rich, and the Ti-rich composition, respectively. Considering the identical device geometry and the same film thickness, the differences were addressed to the different microstructures and different bulk properties of the STO layers. The high effective dielectric permittivity of $\varepsilon_{eff} \approx 85$ was attributed to a higher degree of crystallization in the stoichiometric STO film as compared with nanocrystalline Sr-rich STO ($\varepsilon_{eff} \approx 42$) and partly amorphous Ti-rich STO film ($\varepsilon_{eff} \approx 17$).

Figures 5(a) and 5(b) show representative current-voltage (*I-V*) characteristics of the pristine Pt/STO/TiN crossbar devices measured in the range of ±2.0 V with the voltage signal always applied to the TiN top electrode. A statistical analysis from 30 devices for each sample is shown in Figs. 5(c) and 5(d), respectively, showing the cumulative distribution function (CDF) for the leakage current of the stoichiometric and Ti-rich STO samples measured at +1.0 V and of the higher insulating Sr-rich STO devices measured at +2.0 V.

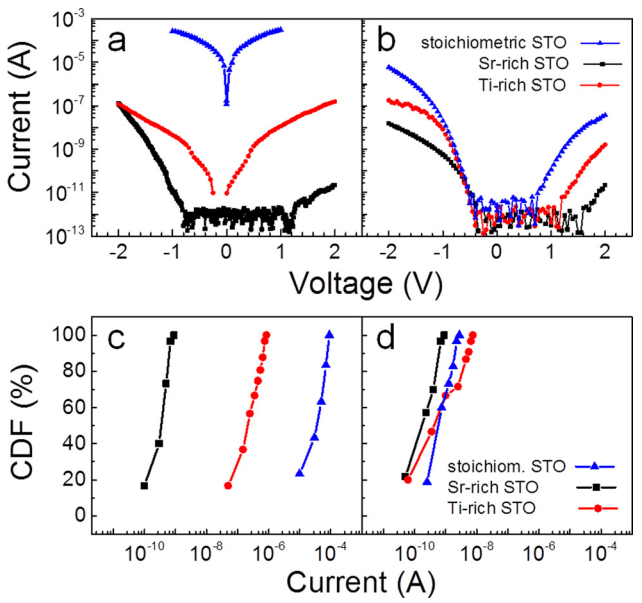

FIG. 5. Current-voltage (*I-V*) characteristics as a function of the STO composition (see Table I) of Pt/STO/TiN devices in pristine state measured at room temperature with the voltage applied to the TiN top electrode. (a) Micro-crossbar devices of 1 μm^2 size made from 15 nm thick polycrystalline STO films and (b) 0.01 μm^2 size nano-crossbar structures with 12 nm thick STO integrated. The CDFs represent the leakage current variations of the (c) micro-crossbar and (d) nano-crossbar devices. The current for the Sr-rich STO films has been measured at +2.0 V, whereas for the stoichiometric and Ti-rich films, the current values were determined at +1.0 V.

1. Micro-crossbar devices

Fig. 5(a) shows the *I-V* plots for micro-crossbar cells of about 1 μm^2 size made from the Sr-rich, stoichiometric, and Ti-rich STO films of about 15 nm thickness annealed at 600 °C for 10 min. The slight asymmetry of the current values with respect to the voltage polarity is attributed to the difference in the work functions of the electrode metals, Pt and TiN, thus giving rise to different Schottky barrier heights of the respective metal/STO interfaces. Although well-defined data for ALD STO/metal interfaces are not available from the literature, the ALD HfO_2/metal system might serve as a reference here. For these interfaces, effective metal work functions of 5.15 eV for Pt[48] and (4.56 ± 0.35) eV for TiN[49] in contact to ALD HfO_2 have been determined revealing a barrier offset of roughly 0.5 eV. From the 50% values of the CDF functions (Fig. 5(c)), mean initial resistances of the micro-crossbar devices were determined being about 5 GΩ for Sr-rich STO, 4 MΩ for Ti-rich STO, and 25 kΩ for the stoichiometric STO. The surprisingly low resistance of the device from stoichiometric STO contradicts the findings reported by other groups.[15,31] This might be attributed to the formation of micro-cracks in the 15 nm thick annealed films which allow an enhanced current flow. The insulating behavior of the Sr-rich devices is in line with the regular dense morphology of the fine-grained films and with the slightly increased band gap found for the Sr-rich STO.[50]

2. Nano-crossbar devices

Fig. 5(b) shows the *I-V* plots for the nano-crossbar devices of 0.01 μm^2 size built from STO films of different compositions which were annealed at 600 °C for 5 min. For the small pad sizes, the current-resolution of the setup of about 1 pA was easily reached at low voltages. The leakage current data of the 12 nm polycrystalline STO films at higher voltages are in reasonable agreement with results reported for high-*k* STO thin films.[15,31] Apparently, the leakage current for the stoichiometric STO films of 12 nm thickness was considerably reduced as compared with the 15 nm thick films (see Fig. 5(a)). This behavior might be attributed to the different microstructures of the films. The SEM micrographs in Figs. 3(b) and 3(e) clearly show that micro-cracks are more pronounced in the 15 nm as compared with the 12 nm film. This might originate either from the variation of the film thickness or the slightly different annealing times, or both. This comparison further supports the assumption that the enhanced current flow in the devices containing stoichiometric STO films was mainly along nano- or micro-cracks rather than along grain boundaries. A statistical analysis of the mean leakage currents of the STO nano-crossbar devices is given in Figure 5(d). The data for the Sr-rich and stoichiometric STO devices are based on a yield of >90%. Thus, mean resistance values of about few 10 GΩ for Sr-rich STO and few GΩ for the stoichiometric STO devices are determined as representative values. The Ti-rich STO nano-crossbar devices show a bigger spread in their initial resistance values ranging from about several GΩ to about 100 MΩ. The type of bimodal device distribution (see Fig. 5(d)) is consistent with the local conductivity distribution determined by LC-AFM (see Fig. 4(g)). Thus for the case of the partly crystallized 12 nm Ti-rich STO films, the nano-crossbar devices might cover different areas of crystalline and amorphous material which results in a larger spread of the initial resistances. For the RS study, we comprised the data of all devices which were formed into the ON state by a positive voltage signal and which were successfully reset to the OFF state by a negative voltage applied to the top electrode.

E. Electroforming of the Pt/STO/TiN devices

The voltage controlled electroforming process[51] was performed for the Pt/STO/TiN devices by applying a positive voltage ramp to the TiN TE with the Pt BE being grounded. To protect the device from hard breakdown, a current compliance I_{cc} for the electroforming procedure was set with values between 10 μA and 100 μA, depending on the leakage current behavior of the investigated cell. Representative electroforming curves for devices of different STO compositions and for two different pad sizes, explicitly 1 μm^2 and 0.01 μm^2, are shown in Figures 6(a) and 6(b), respectively. The voltage at which the abrupt increase in current, the soft breakdown, occurred was identified as the electroforming voltage V_{EF}. Thus, the initially insulating Pt/STO/TiN structure changed into a higher conducting state, which represents voltage-induced electroforming into the ON state. The application of a voltage ramp of opposite polarity resulted in a partial recovery of a high resistivity, thus the device was reset into the OFF state. For the micro-crossbar devices from STO films of different compositions (see Fig. 6(a)), a clear trend of decreasing electroforming voltage with increasing leakage current is observed. This trend was not explicitly

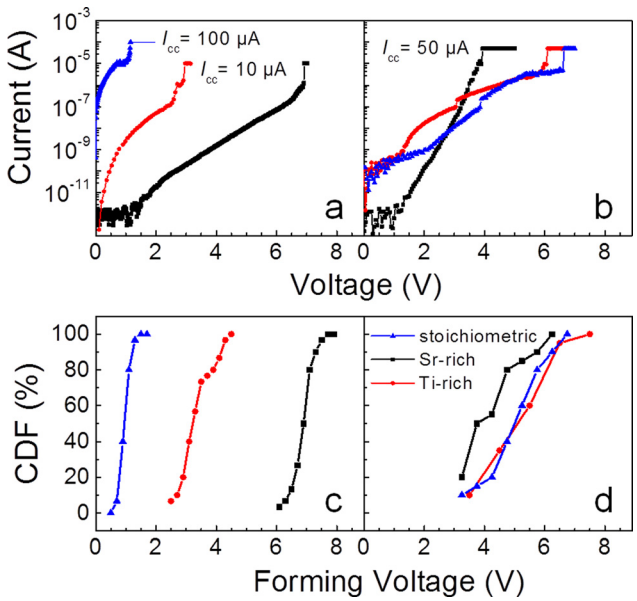

FIG. 6. Representative electroforming *I-V* curves for the (a) micro-crossbar (1 μm^2, 15 nm STO) and (b) nano-crossbar (0.01 μm^2, 12 nm STO) Pt/STO/TiN devices. A positive voltage ramp applied to the TiN top electrode initiated a soft-breakdown event, while the devices were protected by a current compliance I_{cc}. Each CDF was derived from 30 electro-formed (c) micro- and (d) nano-crossbar devices.

repeated in the electroforming behavior of the nano-crossbar devices (Fig. 6(b)), which nevertheless reproduce well the *I-V* curves of the pristine devices for voltages below +2.0 V (see Fig. 5(b)). This observation is attributed to differences in the conduction mechanisms at high fields for the devices built from STO thin films of different compositions and various microstructures.

In summary, all different Pt/STO/TiN devices were electroformed into the ON state when a voltage ramp of positive polarity was applied to the TiN TE. If the samples were afterwards polarized with a negative voltage of about −3.0 V, the high current through the devices was reduced significant, the devices were reset into a higher resistance state, the OFF state. Under subsequent cycling of the voltage signal, the devices showed a hysteretic *I-V* characteristic, i.e., switching between low (LRS = ON) and high resistance (HRS = OFF) state. For each STO thin film sample, statistical analysis for an average of 30 devices formed into the ON state was performed with respect to the electroforming and the RS behavior. Figures 6(c) and 6(d) show the cumulative probability plots of the electroforming voltages (V_{EF}) as a function of the STO composition for 1 μm^2 devices with 15 nm thick STO and 0.01 μm^2 cells with 12 nm thick STO, respectively. For the micro-crossbar cells (Fig. 6(c)), a clear dependency of the films composition on the V_{EF} value is found, with very little variation in V_{EF} for different devices. The mean values were for Sr-rich STO $V_{EF} = 7.0 \pm 1.0$ V, for Ti-rich STO $V_{EF} = 3.5 \pm 1.0$ V, and for stoichiometric STO $V_{EF} = 1.0 \pm 0.5$ V. The electroforming voltages are higher for devices with lower initial leakage currents. Interestingly, for the nano-crossbar devices, a similar effect of the different STO compositions on the electroforming voltage was not observed. However, in comparison with the micro-crossbars, the device-to-device variations in electroforming voltage increased considerably as demonstrated by the non-steep CDF-characteristics in Fig. 6(d). Mean values determined for the various compositions were for Sr-rich STO $V_{EF} = 4.5 \pm 1.5$ V and for stoichiometric and Ti-rich STO $V_{EF} = 5.0 \pm 2.0$ V. Considering the LC-AFM current maps (see Fig. 4), these larger variation of the V_{EF} values for the nano-crossbar structures might be attributed to a device scenario, where the contact pad sizes approach the lateral dimensions of the local conductivity changes of the thin films. This "lateral parameter" can be either the grain size, the distance between small cracks for the Sr-rich and stoichiometric STO films or the distance between the grains for the Ti-rich STO films. From the apparent changes in the CDF-characteristics of V_{EF} (see Figs. 6(c) and 6(d)) which are observed upon changing the crossbar size from "micro" to "nano," we can determine a characteristic length of about a few 100 nm as the distance between local weak spots in the annealed STO thin films. This is in good agreement with the dimensions of the local changes observed in LC-AFM. In summary, the electroforming voltage of Pt/STO/TiN devices is affected by the STO composition in two different ways. The change of the material's stoichiometry affects, intrinsically, the conduction mechanism in the STO film and, extrinsically, the thin film's microstructure and morphology.

F. Resistive switching of Pt/STO/TiN devices

After the electroforming and reset procedures had been carried out, all studied devices exhibited bipolar-type RS behavior. Exemplary, Figures 7(a)–7(c) show the quasi-static *I-V* sweeps obtained for the Pt/STO/TiN nano-crossbar structures with STO films of different compositions. The nano-crossbar devices could be switched at a current compliance of $I_{cc} = 50$ μA with a resistance ratio of $R_{off}/R_{on} > 10$, which is required for ReRAM operation.[19] In addition, Fig. 7(d) shows the endurance plot for the Ti-rich STO nano-crossbar device obtained by repeating 1000 quasistatic switching cycles. At a read voltage of $V_{read} = +0.3$ V the mean values are 15 kΩ for LRS and >3 MΩ for HRS. The micro-crossbar devices showed similar RS characteristics although the quasi-static *I-V* sweeps required a higher current compliance of $I_{cc} = 100$ μA due to the additional leakage component of the larger pads.

All the Pt/STO/TiN crossbar devices exhibited the same polarity of the bipolar switching characteristic. For the *I-V* curves shown in Figs. 7(a)–7(c), the current is plotted against the voltage signal applied to the TiN top electrode. For discussing the polarity in respect of a switching model, the *I-V* hysteresis needs to be referred to the voltage signal at the active switching interface, which for the crossbar cells is the Pt/STO interface. Exemplary, the inset in Fig. 7(c) shows the corresponding *I-V*$_{Pt}$ switching curve with the voltage V_{Pt} applied to the Pt electrode given on the abscissa. Thus, all Pt/STO/TiN crossbar devices exhibit a typical "counter-eightwise" bipolar RS[21] which is characteristic for valence change memories.[5,52]

However, the quasi-static *I-V* sweeps in Figs. 7(a)–7(c) also display differences in the RS behavior of the STO films with different compositions. Remarkably, the Sr-rich STO devices require higher SET-voltages and show stronger

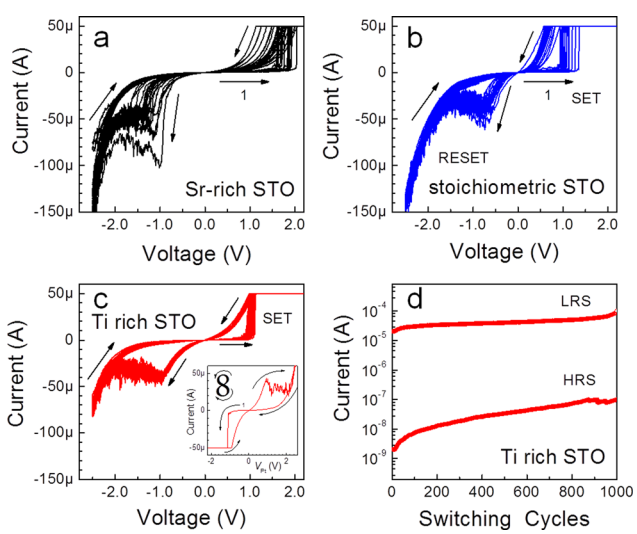

FIG. 7. (a)–(c) *I-V* hysteresis of nano-crossbar Pt/STO/TiN devices of 0.01 μm^2 size with 12 nm polycrystalline STO thin films of different compositions listed in Table I. The voltage signal was applied to the TiN top electrode. All devices reveal a stable bipolar RS at a current compliance of 50 μA. The inset in (c) shows the "counter-eight-wise" RS with respect to the actively switching Pt/STO contact. (d) Endurance plot over 1000 quasi-static switching cycles ($I_{cc} = 100$ μA) for a Pt/Ti-rich STO/TiN device at $V_{read} = +0.3$ V.

variations of the SET-voltages and LRS-currents compared with the stoichiometric and Ti-rich STO nano-crossbar cells. In contrast, the Ti-rich STO devices show the lowest variation in SET-voltages and LRS-currents. These tendencies are also reflected in the switching stability of the devices. Fig. 7(d) shows a stable endurance characteristic for the Ti-rich STO device. The stoichiometric STO cells showed a slightly stronger variation in the LRS and HRS values, whereas the Sr-rich STO devices revealed an LRS degradation towards the OFF-state (not shown here). This feature could be tackled if a higher current compliance for the SET operation was adjusted. However, the objective of this study was to investigate the effect of the STO film composition for nearly identical devices measured under the same conditions.

The differences appearing in the RS behavior of the various STO samples might be explained by a variation in the "strength" of the conductive filament which is formed during the SET-process. This description is supported by differences in the LRS non-linearity (NL). The non-linearity factor *NL* is calculated from the RESET-characteristic according to $NL = |I(V_{RESET})|/|I(V_{RESET}/2)|$.[53] For the characteristics of the stoichiometric STO and Ti-rich STO devices, this definition yields *NL*-values between 4 and 7. In contrast, significantly higher values of $NL = (18 \pm 5)$ are calculated for the Sr-rich STO cells if operated under identical conditions ($I_{cc} = 50\ \mu A$, $V_{RESET,stop} = -2.5\ V$). In general, a higher *NL*-value of the LRS state is considered as an indication for a weaker filament in the ON-state. The effect of a "weaker" ON-state filament formed in the Sr-rich STO thin films in comparison with the stoichiometric and Ti-rich compositions can be interpreted as a difference in the redox-chemical processes involved in the VCM-type RS behavior.

For a broader discussion, the RS characteristics of the various STO devices have been analyzed in a statistical manner for two device sizes, i.e., 1 μm^2 and 0.01 μm^2, and three STO compositions, i.e., [Sr]/([Sr] + [Ti]) ratios of 0.57 (Sr-rich), 0.50 (stoichiometric), and 0.46 (Ti-rich). The variation of the data determined from about 20 devices and 30 switching cycles per device is described by means of the CDF. Characteristic values of the *I-V* hysteresis (see Figs. 7(a)–7(c) for comparison) to be discussed are: (1) the SET-voltage V_{SET}, determined as the voltage, where the current compliance is reached during the (abrupt) SET-process, (2) the RESET-voltage V_{RESET}, determined as the voltage where the negative current reaches a local maximum during RESET –process, and (3) the resistance values R_{ON} (LRS) and R_{OFF} (HRS) determined at a read voltage $V_{read} = +0.3\ V$. It should be re-emphasized that the maximum current at SET-operation was limited by a current compliance with values of $I_{cc} = 100\ \mu A$ for the micro-crossbar and 50 μA for the nano-crossbar structures. The RESET stop biasing was defined at $V_{RESET,stop} = -2.5\ V$.

1. SET- and RESET-voltages

Figure 8 shows the CDF of the SET- and RESET-voltages of the STO based RS devices for (a) the 1 μm^2 micro-crossbars and (b) the 0.01 μm^2 nano-crossbars. The three STO compositions are again encoded by colors (see Fig. 7). The micro-crossbar cells reveal rather narrow distributions of the switching voltages and quite symmetric values for V_{SET} and V_{RESET}, in contrast to the nano-crossbar devices. The micro-crossbar devices with non-stoichiometric STO films show slightly larger SET-voltages compared with the values of the RESET-voltages. For the Ti-rich STO, mean values are $V_{SET} \approx 0.85 \pm 0.1\ V$ and $|V_{RESET}| \approx 0.65 \pm 0.15\ V$, and for the Sr-rich STO, we obtain $V_{SET} \approx 1.0 \pm 0.15\ V$ and $|V_{RESET}| \approx 0.9 \pm 0.1\ V$. In contrast, the switching voltages of the stoichiometric STO cells are nearly symmetric with absolute values of $V_{SET} \approx |V_{RESET}| \approx (0.9 \pm 0.1)\ V$. Remarkably, the switching voltages of the different micro-crossbar devices are very close in contrast to the forming voltages which differ significantly for the various STO compositions (see Fig. 6(c)). Additionally, it is found that the stoichiometric STO devices with the highest leakage current in the initial state (see Fig. 5(a)) show a nearly forming-free RS behavior, i.e., $V_{FORM} \approx V_{SET} \approx 1.0\ V$.

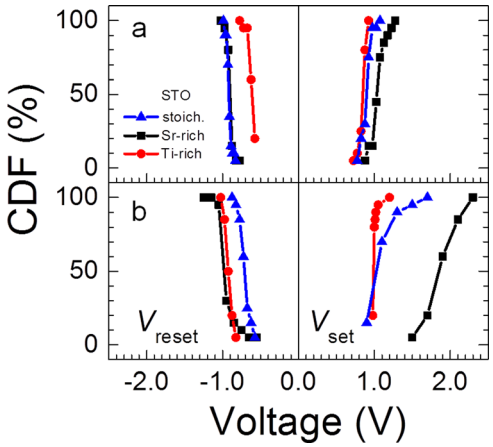

FIG. 8. Cumulative distribution functions of the SET- and RESET-voltages of the quasistatic *I-V* hystereses for (a) micro-crossbar (1 μm^2 size, 15 nm thick STO) and (b) nano-crossbar (0.01 μm^2 size, 12 nm thick STO) Pt/STO/TiN devices of different compositions listed in Table I.

A relation between higher initial leakage and lower forming voltage has also been reported for HfO_2-based RS devices.[9] From the correlation of morphological and LC-AFM studies, we suggest that the RS switching in the polycrystalline STO films might dominantly appear at weak points like, for example, the observed micro-cracks. This brings up the question whether the RS in the ALD STO based devices is a filamentary-type phenomenon or somehow relates to the density of micro-cracks in the thin films. This point will be further addressed at the end of the section.

For the nano-crossbar cells shown in Fig. 8(b), in general, the SET-voltages $|V_{SET}|$ were higher than the corresponding $|V_{RESET}|$-values. Here, the Ti-rich STO films show the most symmetric RS curves with $V_{SET} \approx 1.0 \pm 0.15\ V$ and $|V_{RESET}| \approx 0.95 \pm 0.1\ V$. In contrast, the stoichiometric STO devices with $V_{SET} \approx 1.1 \pm 0.4\ V$ and $|V_{RESET}| \approx 0.7 \pm 0.15\ V$, and the Sr-rich STO with $V_{SET} \approx 1.9 \pm 0.4\ V$ and $|V_{RESET}| \approx 1.0 \pm 0.2\ V$ exhibit a significant asymmetry in the RS behavior.

An increase in the SET- and RESET-voltages with decreasing device size has also been reported for HfO_2-based RS devices by Chen *et al.*,[8] who addressed this effect to the

lower total number of defects in the smaller devices compared with the larger ones. This scenario might also apply to the STO based RS devices in this study. Interestingly, the analysis of the influence of the [Sr]/([Sr] + [Ti]) composition on the switching voltages revealed the same trends for the micro- and nano-crossbar cells, i.e., an increase in the mean switching voltage with increasing Sr-content in the STO thin films. This stoichiometry effect is especially pronounced for the nano-crossbar cells, which have been switched at a low current compliance of 50 μA.

Notable for the nano-crossbars is the variation in the distributions of SET-voltages. The Ti-rich STO nano-crossbar devices exhibit a rather narrow distribution of the SET-voltages with a variation of ($\pm$0.15 V) and a nearly symmetric *I-V* characteristic. In contrast, the stoichiometric STO and the Sr-rich STO cells both show a much stronger variation of the SET-voltages in the range of ($\pm$0.4 V) in combination with a significant asymmetry of the switching curves, which is stronger for the Sr-rich STO ($|V_{SET}| - |V_{RESET}| = 0.9$ V) than for the stoichiometric STO sample ($|V_{SET}| - |V_{RESET}| = 0.4$ V).

The differences in the RS characteristics of the STO-based devices of various [Sr]/([Sr] + [Ti]) compositions might be interpreted by a stoichiometry effect on the redox-reactions taking place during SET and RESET process leading to a closing and opening of the conductive filament, respectively. The RS behavior of the Sr-rich STO devices, in comparison with the other compositions, is characterized by a higher forming voltage, a higher SET-voltage, a larger variation in the SET-voltages and in the LRS behavior, and a higher LRS non-linearity. These observations can be consistently described under the assumption that the reduction process which leads to the SET of the conducting filament is impeded for the Sr-rich STO devices, while for stoichiometric and Ti-rich STO films, it is quite similar.

The observed effects in the RS behavior of nano-crystalline ALD grown STO thin films as a function of the [Sr]/[Sr] + [Ti] composition are in reasonable agreement with the microscopic description of the films given in Sec. III A. For XPS data, the possibility of SrO intergrowth for the Sr-rich STO films has been suggested while any differences between the stoichiometric and the Ti-rich STO films were not obtained. For the constituents of $SrTiO_3$, the standard free energies of formation of oxides ΔG^0 obtained from the Ellingham diagram[54] differ significantly, i.e., $|\Delta G^0(SrO)| \gg |\Delta G^0(TiO_2)|$ at a given conditions. Therefore, the SrO intergrowth found for the Sr-rich STO films might impede local reduction reactions resulting in a lower concentration of oxygen vacancies and therefore in a weaker conductive filament. This gives rise to a higher resistance in LRS, a higher LRS-NL, and a stronger variation of the LRS resistance. In contrast, the small $|\Delta G^0(TiO_2)|$ value for TiO_2 might enable easy reduction of the stoichiometric and Ti-rich STO films resulting in a low SET-voltage and stable SET-operation and LRS characteristics.

2. ON- and OFF-resistance states

Figure 9 shows the CDF plots of the ON-state (LRS) and OFF-state (HRS) resistance values for the STO based

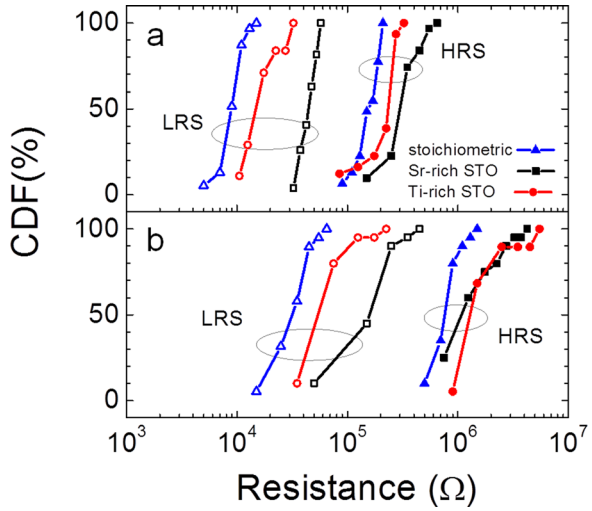

FIG. 9. Cumulative distribution functions of the resistance values derived from the quasistatic *I-V* hystereses for (a) micro-crossbar (1 μm^2 size, 15 nm thick STO) and (b) nano-crossbar (0.01 μm^2 size, 12 nm thick STO) Pt/STO/TiN devices of different compositions (see Table I).

RS devices determined from continuous *I-V* switching cycles at a read voltage of $V_{read} = +0.3$ V. Again, the three STO compositions are encoded by colors and the data for the micro- and nano-crossbars are shown in Figs. 9(a) and 9(b), respectively. General trends which can be identified are, first, that smaller devices exhibit higher LRS- and HRS-values, and second, that the data spread as a function of the [Sr]/([Sr] + [Ti]) composition is larger for the LRS values as compared with the HRS values. In addition, for each device size, the stoichiometric STO cells show the lowest resistance values in ON- and OFF-state compared with the values of the non-stoichiometric STO devices.

3. Area-dependency

In order to assess the influence of the device size, the area dependency of the resistance values for the devices of different STO compositions has been analyzed. The graph in Figure 10 comprises mean values of the HRS (filled symbols) and the LRS (open symbols) for four different device sizes, i.e., 0.01 μm^2, 1 μm^2, 25 μm^2, and 100 μm^2. The micro-crossbar devices (>1 μm^2) were fabricated from STO films of about 15 nm thickness, while for the nano-crossbar devices (0.01 μm^2), films of about 12 nm were integrated. The different STO compositions are again encoded by the colors. Despite the different film thicknesses and crossbar-structures, a quite consistent trend in the resistance values as a function of the device size is obtained for the devices of different STO compositions. The higher resistance values obtained for the nano-crossbar devices can be ascribed to modified measurement conditions, i.e., the lower current compliance defined for the SET processes of the nano-crossbar devices. The area-dependency of the micro-crossbar devices can be summarized as follows: The Sr-rich STO devices (black) show a very weak area dependency for the LRS and HRS values. A resistance ratio $R_{OFF}^{Sr-STO}/R_{ON}^{Sr-STO} \simeq 10$ independent of the device area was determined which is addressed to the high insulating properties of the annealed

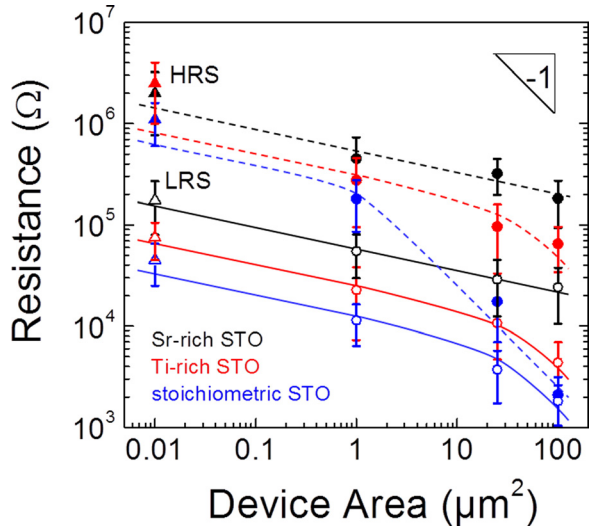

FIG. 10. Area dependency of the resistance states of the Pt/STO/TiN devices determined at $V_{read} = +0.3$ V from stable, quasistatic *I-V* hystereses. The colors encode the films composition, Sr-rich (black), Ti-rich (red), and stoichiometric STO (blue) values (see Table I), resistance values of LRS/HRS are given in open/filled symbols. The symbols stand for the different structures, circles for micro-crossbars ($I_{cc} = 100\,\mu$A), and triangles for nano-crossbars ($I_{cc} = 50\,\mu$A). The slope of (−1) is plotted for easier identification of area-scaling.

Sr-rich STO thin films. The Ti-rich STO devices also show a weak area-dependency of the LRS, while the resistance values are reduced to about one third compared with Sr-rich STO, $R_{ON}^{Ti-STO}/R_{ON}^{Sr-STO} \approx 1/3$. The HRS values of the Ti-rich STO reveal an enhanced dependency on the cell area which is attributed the higher leakage currents becoming significant for larger devices, whereas a mean resistance ratio $R_{OFF}^{Ti-STO}/R_{ON}^{Ti-STO} \simeq 20$ is obtained for the smaller devices ($\leq 10\,\mu m^2$). For small cells ($\leq 1\,\mu m^2$), the stoichiometric STO devices show a weak area dependence for the LRS and HRS values with a resistance ratio $R_{OFF}^{stoi-STO}/R_{ON}^{stoi-STO} \simeq 25$, while for device sizes $>1\,\mu m^2$, the HRS values show a strong area dependence with a proportionality factor of approximately one. This clearly demonstrates that here the effect of leakage current along the micro-cracks (see Fig. 3(b)) dominates the total current for large pad sizes. For the $>10\,\mu m^2$-size stoichiometric STO devices, any RS effect is completely obscured by the high leakage current contribution from the non-switching area of the device. As a consequence, reliable information on the compositional effect of the ALD STO films on the RS properties can only be obtained from device structures with reasonably small sizes.

In LRS, all STO devices of the three compositions show a considerably weak area-dependency of their resistance values. This is interpreted in the way that the area-independent VCM-type filamentary mechanism dominates the RS characteristics of the Pt/STO/TiN devices after electroforming. The area-dependency of the HRS values demonstrates the important effect of the film's microstructure and morphology on the RS properties. Overlying the area-dependency, also an effect of the STO thin film composition is observed, predominantly for the LRS states. Considering devices of the same size, smaller than $10\,\mu m^2$, the ON-state resistance values increase from stoichiometric to Ti-rich to Sr-rich STO films resulting in a ratio of the LRS values $R_{ON}^{Sr-STO}/R_{ON}^{stoi-STO} \approx 6$. Although the HRS states of the smaller devices are not too much affected by an area dependent leakage current parallel to the filament current, the dependence of the HRS states on the composition of the STO films is less pronounced. Especially when the RS cell is in insulating state defects might have a considerable influence on the total (HRS) resistance. However, the highest resistance ratio R_{OFF}/R_{ON} of about 25 was obtained for stoichiometric STO and the lowest value of about 10 for the Sr-rich STO films.

In addition to the significant influence of the STO thin films microstructure on the RS characteristics of respective Pt/STO/TiN devices, also a composition effect was observed. While micro-structural effects (e.g., micro-cracks and grain sizes) dominate the resistance states for larger cell areas, the HRS states of the nano-crossbar cells might still be affected by varying defect densities in the films induced by differences in the films crystallization behavior. However, the LRS values of the Pt/STO/TiN devices show a reproducible tendency with variation of the STO film composition: $R_{ON}^{Sr-STO} > R_{ON}^{Ti-STO} \geq R_{ON}^{stoi-STO}$, for different device sizes, film thicknesses, and microstructures. This finding might indicate a compositional dependence of the local defect states of the conducting filaments in RS devices from polycrystalline ALD STO thin films with various [Sr]/([Sr] + [Ti]) contents.

IV. CONCLUSIONS

In this study, we investigated the RS properties of Pt/STO/TiN devices from ALD derived $Sr_{1+x}Ti_{1+y}O_{3+(x+2y)}$ thin films of various compositions. Metastable perovskite STO films were grown on platinum coated silicon substrates by ALD at 350 °C using cyclopentadienyl-based metal precursors and oxygen plasma and a subsequent annealing at 600 °C in N_2. STO films of 15 nm and 12 nm thickness and with three different compositions [Sr]/([Sr] + [Ti]) of 0.57 (Sr-rich), 0.50 (stoichiometric), and 0.46 (Ti-rich) were integrated into crossbar-devices with lateral dimensions varied from $(10 \times 10)\ \mu m^2$ to $(100 \times 100)\ nm^2$. Nano-structural characterizations by means of SEM and LC-AFM revealed a significant influence of the STO cation composition on the crystallization behavior and, thus, on the resulting morphologies of the ALD films. Local defects in the film's microstructure dominantly affect the leakage current behavior of pristine Pt/STO/TiN cells and their soft-breakdown or electroforming voltages. For cell sizes $>1\,\mu m^2$ the HRS of the RS characteristics is superimposed by residual cell conductivity. The polarity dependence of the RS curves and the area-independent LRS values serve as a direct proof of VCM-type filamentary RS taking place in the Pt/STO/TiN devices under study. Once the microstructural effects of the polycrystalline thin films have been assessed, a clear effect of the STO composition on the RS behavior was observed. Nano-crossbar devices from stoichiometric STO films could be switched at lowest voltages of about 1.0 V between the lowest LRS values of $R_{ON} \approx 40\,k\Omega$ and reasonable HRS values of $R_{OFF} \approx 1$ MΩ determined at +0.3 V. Non-

stoichiometry in the ALD grown STO films, especially Sr-excess, increases the devices R_{ON} values, i.e., result in LRS of lower conductance.

ACKNOWLEDGMENTS

This work has been supported in parts by the European Community's Seventh Framework Programme (FP7/2007-2013) under Grant Agreement No. ENHANCE- 238409 and by the Deutsche Forschungsgemeinschaft (SFB 917). The authors thank Florian Lentz, Marcel Reiners, René Borowski, Hans-Peter Bochem, and Wytze Keuning for their support and fruitful discussions.

[1]ITRS-The International Technology Roadmap for Semiconductors, http://www.itrs.net/, 2012.
[2]S. Yu, B. Gao, Z. Fang, H. Yu, J. F. Kang, and H.-S. P. Wong, Adv. Mater. **25**, 1774 (2013).
[3]R. Bruchhaus, R. Muenstermann, T. Menke, C. Hermes, F. Lentz, R. Weng, R. Dittmann, and R. Waser, Curr. Appl. Phys. **11**, E75 (2011).
[4]H. D. Lee, S. G. Kim, K. Cho, H. Hwang, H. Choi, J. Lee, S. H. Lee, H. J. Lee, J. Suh, S. Chung, Y. S. Kim, K. S. Kim, W. S. Nam, J. T. Cheong, J. T. Kim, S. Chae, E. Hwang, S. N. Park, Y. S. Sohn, C. G. Lee, H. S. Shin, K. J. Lee, K. Hong, H. G. Jeong, K. M. Rho, Y. K. Kim, S. Chung, J. Nickel, J. J. Yang, H. S. Cho, F. Perner, R. S. Williams, J. H. Lee, S. K. Park, and S. Hong, Symp. VLSI Technol. **2012**, 151.
[5]R. Waser, R. Bruchhaus, and S. Menzel, in *Nanoelectronics and Information Technology*, 3rd ed., edited by R. Waser (Wiley-VCH, 2012), p. 683.
[6]Y. Chen, B. Govoreanu, L. Goux, R. Degraeve, A. Fantini, G. Kar, D. Wouters, G. Groeseneken, J. Kittl, M. Jurczak, and L. Altimime, IEEE Trans. Electron Devices **59**, 3243 (2012).
[7]S. Stille, C. Lenser, R. Dittmann, A. Koehl, I. Krug, R. Muenstermann, J. Perlich, C. M. Schneider, U. Klemradt, and R. Waser, Appl. Phys. Lett. **100**, 223503 (2012).
[8]Y. Y. Chen, L. Goux, L. Pantisano, J. Swerts, C. Adelmann, S. Mertens, V. V. Afanas'ev, X. P. Wang, B. Govoreanu, R. Degraeve, S. Kubicek, V. Paraschiv, B. Verbrugge, N. Jossart, L. Altimime, M. Jurczak, J. Kittl, G. Groeseneken, and D. J. Wouters, Microelectron. Eng. **112**, 92 (2013).
[9]M. Lanza, G. Bersuker, M. Porti, E. Miranda, M. Nafria, and X. Aymerich, Appl. Phys. Lett. **101**, 193502 (2012).
[10]Y. Wu, S. Yu, B. Lee, and P. Wong, J. Appl. Phys. **110**, 094104 (2011).
[11]K. Kim, S. Han, and C. Hwang, Nanotechnology **23**, 035201 (2012).
[12]S. J. Park, J. P. Lee, J. S. Jang, H. Rhu, H. Yu, B. Y. You, C. S. Kim, K. J. Kim, Y. J. Cho, S. Baik, and W. Lee, Nanotechnology **24**, 295202 (2013).
[13]K. Szot, M. Rogala, W. Speier, Z. Klusek, A. Besmehn, and R. Waser, Nanotechnology **22**, 254001 (2011).
[14]M. Rogala, Z. Klusek, C. Rodenbücher, R. Waser, and K. Szot, Appl. Phys. Lett. **102**, 131604 (2013).
[15]N. Menou, M. Popovici, S. Clima, K. Opsomer, W. Polspoel, B. Kaczer, G. Rampelberg, K. Tomida, M. A. Pawlak, C. Detavernier, D. Pierreux, J. Swerts, J. W. Maes, D. Manger, M. Badylevich, V. V. Afanas'ev, T. Conard, P. Favia, H. Bender, B. Brijs, W. Vandervorst, S. Van Elshocht, G. Pourtois, D. J. Wouters, S. Biesemans, and J. A. Kittl, J. Appl. Phys. **106**, 094101 (2009).
[16]R. Waser, R. Dittmann, G. Staikov, and K. Szot, Adv. Mater. **21**, 2632 (2009).
[17]R. Muenstermann, T. Menke, R. Dittmann, S. Mi, C.-L. Jia, D. Park, and J. Mayer, J. Appl. Phys. **108**, 124504 (2010).
[18]S. Menzel, M. Waters, A. Marchewka, U. Böttger, R. Dittmann, and R. Waser, Adv. Funct. Mater. **21**, 4487 (2011).
[19]R. Waser and M. Aono, Nature Mater. **6**, 833 (2007).
[20]K. Szot, W. Speier, G. Bihlmayer, and R. Waser, Nature Mater. **5**, 312 (2006).
[21]R. Muenstermann, T. Menke, R. Dittmann, and R. Waser, Adv. Mater. **22**, 4819 (2010).
[22]A. Koehl, D. Kajewski, J. Kubacki, C. Lenser, R. Dittmann, P. Meuffels, K. Szot, R. Waser, and J. Szade, Phys. Chem. Chem. Phys. **15**, 8311 (2013).
[23]K. Shibuya, S. Mi, C. L. Jia, P. Meuffels, and R. Dittmann, Appl. Phys. Lett. **92**, 241918 (2008).
[24]U. Schroeder, H. Schroeder, A. Kingon, S. Summerfelt, C. S. Hwang, and U. Boettger, in *Nanoelectronics and Information Technology*, 3rd ed., edited by R. Waser (Wiley-VCH, 2012), p. 635.
[25]S. K. Kim, S. W. Lee, J. H. Han, B. Lee, S. Han, and C. S. Hwang, Adv. Funct. Mater. **20**, 2989 (2010).
[26]M. Lukosius, T. Blomberg, D. Walczyk, G. Ruhl, and Ch. Wenger, IOP Conf. Ser.: Mater. Sci. Eng. **41**, 012015 (2012).
[27]T. Blomberg, J. Anttila, S. Haukka, M. Tuominen, M. Lukosius, Ch. Wenger, and T. Saukkonen, Thin Solid Films **520**, 6535 (2012).
[28]C. Jorel, C. Valle, P. Gonon, E. Gourvest, C. Dubarry, and E. Defay, Appl. Phys. Lett. **94**, 253502 (2009).
[29]M. Lukosius, C. Wenger, T. Blomberg, and G. Ruhl, J. Vac. Sci. Technol., B **31**, 01A102 (2013).
[30]C. S. Hwang, Mater. Sci. Eng., B **56**, 178 (1998).
[31]W. Lee, J. H. Han, W. Jeon, Y. W. Yoo, S. W. Lee, S. K. Kim, C. H. Ko, C. Lansalot-Matras, and C. S. Hwang, Chem. Mater. **25**, 953 (2013).
[32]M. Popovici, S. Van Elshocht, N. Menou, P. Favia, H. Bender, E. Rosseel, J. Swerts, C. Adelmann, C. Vrancken, A. Moussa, H. Tielens, K. Tomida, M. Pawlak, B. Kaczer, G. Schoofs, W. Vandervorst, D. Wouters, and J. Kittl, J. Vac. Sci. Technol., B **29**, 01A304 (2011).
[33]S. Yu, H.-Y. Chen, B. Gao, J. Kang, and H.-S. P. Wong, ACS Nano **7**, 2320 (2013).
[34]V. Longo, M. A. Verheijen, F. Roozeboom, and W. M. M. Kessels, ECS J. Solid State Sci. Technol. **2**, N120 (2013).
[35]V. Longo, N. Leick, F. Roozeboom, and W. M. M. Kessels, ECS J. Solid State Sci. Technol. **2**, N15 (2013).
[36]D. Briggs and M. P. Seah, *Practical Surface Analysis: Auger and X-ray Photoelectron Spectroscopy*, 2nd ed. (John Wiley & Sons, New York, 1990).
[37]V. Longo, F. Roozeboom, W. M. M. Kessels, and M. A. Verheijen, ECS Trans. **58**, 153 (2013).
[38]S. Witek, D. M. Smyth, and H. Pickup, J. Am. Ceram. Soc. **67**, 372 (1984).
[39]G. J. McCarthy, W. B. White, and R. Roy, J. Am. Ceram. Soc. **52**, 463 (1969).
[40]R. Tilley, J. Solid State Chem. **21**, 293 (1977).
[41]K. Szot and W. Speier, Phys. Rev. B: Condens. Matter **60**, 5909 (1999).
[42]M. Fujimoto and M. Watanabe, J. Mater. Sci. **20**, 3683 (1985).
[43]N. A. Benedek, C. Elsaesser, and M. W. Finnis, J. Phys.: Conf. Ser. **94**, 012005 (2008).
[44]S. Clima, G. Pourtois, N. Menou, M. Popovici, A. Rothschild, B. Kaczer, S. Van Elshocht, X. P. Wang, J. Swerts, D. Pierreux, S. DeGendt, D. J. Wouters, and J. A. Kittl, Microelectron. Eng. **86**, 1936 (2009).
[45]K. Shibuya, R. Dittmann, S. Mi, and R. Waser, Adv. Mater. **22**, 411 (2010).
[46]B. Psiuk, J. Szade, H. Schroeder, H. Haselier, M. Mlynarczyk, R. Waser, and K. Szot, Appl. Phys. A-Mater. Sci. Process. **89**, 451 (2007).
[47]D. Kajewski, R. Wrzalik, M. Wojtyniak, M. Pilch, J. Szade, K. Szot, Ch. Lenser, R. Dittmann, and R. Waser, Phase Transitions **84**, 483 (2011).
[48]D. Gu, S. K. Dey, and P. Majhi, Appl. Phys. Lett. **89**, 082907 (2006).
[49]R. K. Pandey, R. Sathiyanarayanan, U. Kwon, V. Narayanan, and K. V. R. M. Murali, J. Appl. Phys. **114**, 034505 (2013).
[50]N. Aslam, V. Longo, W. Keuning, F. Roozeboom, W. M. M. Kessels, R. Waser, and S. Hoffmann-Eifert, Phys. Status Solidi **211**, 389 (2014).
[51]D. S. Jeong, H. Schroeder, U. Breuer, and R. Waser, J. Appl. Phys. **104**, 123716 (2008).
[52]D. Jeong, R. Thomas, R. Katiyar, J. Scott, H. Kohlstedt, A. Petraru, and C. Hwang, Rep. Prog. Phys. **75**, 076502 (2012).
[53]F. Lentz, B. Roesgen, V. Rana, D. J. Wouters, and R. Waser, IEEE Electron Device Lett. **34**, 996 (2013).
[54]T. B. Reed, *Free Energy of Formation of Binary Compounds: An Atlas of Charts for High-Temperature Chemical Calculations* (MIT Press, 1972).